High precision detection of change in intermediate range order of amorphous zirconia-doped tantala thin films due to annealing

K. Prasai,[1,*] J. Jiang,[2] A. Mishkin,[2] B. Shyam,[3] S. Angelova,[4] R. Birney,[4] D. A. Drabold,[5] M. Fazio,[6] E. K. Gustafson,[7] G. Harry,[8] S. Hoback,[8] J. Hough,[9] C. Lévesque,[10] I. MacLaren,[9] A. Markosyan,[1] I. W. Martin,[9] C. S. Menoni,[6] P. G. Murray,[9] S. Penn,[11] S. Reid,[4] R. Robie,[9] S. Rowan,[9] F. Schiettekatte,[10] R. Shink,[10] A. Turner,[9] G. Vajente,[7] H-P. Cheng,[2] M. M. Fejer,[1] A. Mehta,[12] and R. Bassiri[1,†]

[1]*E. L. Ginzton Laboratory, Stanford University, Stanford, California 94305, USA*
[2]*Department of Physics and Quantum Theory Project, University of Florida, Gainesville, Florida 32611, USA*
[3]*University of Dayton Research Institute, Dayton, Ohio 45469, USA*
[4]*SUPA, Department of Biomedical Engineering, University of Strathclyde, Glasgow G1 1QE, United Kingdom*
[5]*Department of Physics and Astronomy, Ohio University, Athens, Ohio 45701, USA*
[6]*Department of Electrical and Computer Engineering, Colorado State University, Fort Collins, Colorado 80523, USA*
[7]*LIGO Laboratory, California Institute of Technology, Pasadena, California 91125, USA*
[8]*Department of Physics, American University, Washington, DC 20016, USA*
[9]*SUPA, School of Physics and Astronomy, University of Glasgow, Glasgow G12 8QQ, UK*
[10]*Department of Physics, Université de Montréal, Québec H3T 1J4, Canada*
[11]*Department of Physics, Hobart and William Smith Colleges, Geneva, New York 14456, USA*
[12]*SLAC National Accelerator Laboratory, Menlo Park, California 94025, USA*

(Dated: July 31, 2019)

Understanding the local atomic order in amorphous thin film coatings and how it relates to macroscopic performance factors, such as mechanical loss, provides an important path towards enabling the accelerated discovery and development of improved coatings. High precision X-ray scattering measurements of thin films of amorphous zirconia-doped-tantala (ZrO_2-Ta_2O_5) show systematic changes in intermediate range order (IRO) as a function of post-deposition heat-treatment (annealing). Atomic modeling captures and explains these changes, and shows that the material has building blocks of metal-centered polyhedra and the effect of annealing is to alter the connections between the polyhedra. The observed changes in IRO are associated with a shift in the ratio of corner-sharing to edge-sharing polyhedra. These changes correlate with changes in mechanical loss upon annealing, and suggest that the mechanical loss can be reduced by developing a material with a designed ratio of corner-sharing to edge-sharing polyhedra.

Amorphous thin film coatings are technologically important materials that often limit the performance of a variety of precision measurements. For example, Brownian thermal noise, due to mechanical loss in thin film coatings, is a significant impairment in atomic clocks [1] and interferometric gravitational-wave detectors [2], such as the Laser Interferometer Gravitational-wave Observatory (LIGO), Virgo and KAGRA. It is of critical importance to future generations of interferometric gravitational-wave detectors [3] to develop thin-film coatings with lower mechanical loss, and hence lower Brownian thermal noise. For the Advanced LIGO + upgrade, due to start installation in 2022, a coating with a four-fold improvement in mechanical loss is desired, which together with frequency dependent squeezing would enable an eight-fold increase in the volume of the Universe observable by gravitational waves [4, 5].

Post-deposition annealing of amorphous thin films has been shown to induce changes in both the atomic structure and mechanical loss [6, 7]. Annealing tantala up to 600°C, prior to the onset of crystallization, reduces the room temperature mechanical loss of the coatings [8]. Doping tantala with zirconia can suppress crystallization, allowing thin-films to remain amorphous after annealing up to 800°C [9]. For the zirconia-doped tantala studied here, the mechanical loss of an as-deposited film of $\sim 1 \times 10^{-3}$ significantly decreases to 1.8×10^{-4} upon annealing at 800°C [10], which is somewhat below the titania-doped tantala currently employed in Advanced LIGO. This result demonstrates that zirconia-doped tantala is a promising coating material system that warrants further study as a potential Advanced LIGO + mirror coating.

The local atomic order in amorphous materials often governs its macroscopic properties, such as mechanical loss. It is therefore of interest to measure the local atomic order, and identify the key atomic structure motifs that govern macroscopic properties. However, obtaining an accurate measurement of the local order is challenging, especially in thin-films. In this letter, we address this challenge and measure with high precision subtle changes in local order as a function of post-deposition annealing of zirconia-doped tantala thin films. We use grazing-incidence pair distribution function (GIPDF) measurements and atomic structure modeling that captures the local order changes accurately up to 15 Å. Finally, we

discuss the implications of this increased understanding of the atomic structure and its relation to our efforts to reduce mechanical loss.

In general, the atomic structure of amorphous materials can be described in terms of short- and intermediate-range order (SRO and IRO, respectively); the long-range order (LRO), characteristic of crystals, is unambiguously absent [11, 12]. SRO generally describes the structural order up to the first coordination sphere measured as the first peak in the PDF, which often resembles the amorphous material's crystalline counterpart. For zirconia-doped tantala, we choose, among the various definitions of SRO [13], order up to ~ 2.9 Å, which is where the first coordination polyhedra of the material end. The IRO describes the structural organization that is *intermediate* between the discrete chemical bonds described in the SRO and the periodic lattice described in the LRO. However, the IRO is less well understood than the SRO, and is more dependent on the details of how the material was synthesized or deposited.

The structural changes associated with post-deposition annealing are often observed beyond the first coordination sphere, and lie in the IRO [14]. Even with tools that are best suited to probe the IRO, such as fluctuation electron microscopy (FEM) and X-ray or neutron PDFs, the observed structural changes can be small and difficult to interpret. Accurate atomic modeling is required to capture the small changes in the atomic structure, and probe the IRO in detail.

GIPDF data was collected from thin films of zirconia-doped tantala deposited by MLD Technologies (Mountain View, CA), by ion-beam sputtering with a $\mathrm{Zr/(Zr+Ta)} \simeq 0.48$, ~ 590 nm in thickness on fused silica substrates [10]. The target materials were pure metals in a partially pressurized oxygen environment, and the ambient temperature during deposition was less than 100°C. Post-deposition annealing in air of three different samples was carried out at 300, 600 and 800°C. GIPDF data was collected at the dedicated X-ray scattering beamline 10-2 at the Stanford Synchrotron Radiation Lightsource (SSRL). This unique GIPDF capability allows us to overcome a significant difficulty in measuring PDFs from thin films: a grazing incidence angle can be chosen that enables the collection of X-rays scattered from the coatings and not the substrate while maintaining a relatively high q-range of 20.1 $\mathrm{Å}^{-1}$. In addition, there is no destructive sample preparation, ensuring that the observed changes in the measured atomic structure do not result from the sample preparation process, which is especially relevant when looking at small structural changes due to annealing. Further details on the GIPDF data collection method and its merits, in particular pertaining to doped tantala coatings is discussed in [15]. The total scattering data was reduced to the normalized structure factor $\mathrm{S}(q)$ after applying identical corrections on all samples for air scattering, absorption, Compton scattering, polarization effects and geometric effects due to the detector footprint [15, 16].

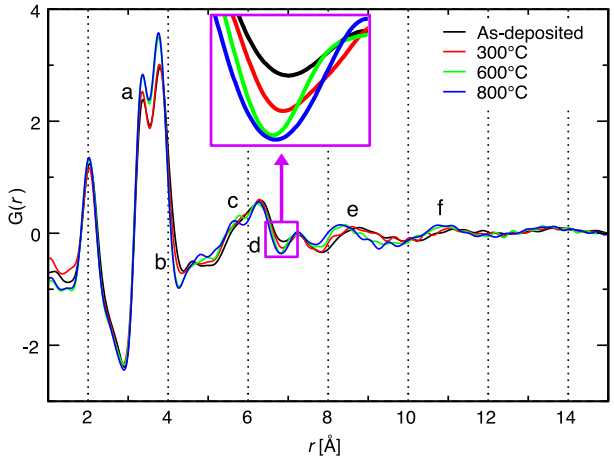

FIG. 1. **Detection of annealing induced changes:** Measured GIPDFs of zirconia-doped tantala thin films. The thin films differed only in annealing history: as-deposited, 300, 400, 600 and 800°C. The differences among the PDFs are the result of annealing-induced change to the atomic structure. The letters represent sections of PDF where the most significant changes are observed: (a), (b) and (d) change in intensity, (c) new peaks appearing, (e) and (f) shift in peak positions. Section (d) is magnified in the inset to highlight the systematic change as a function of annealing temperature.

The measured PDFs for an as-deposited and the three annealed samples are plotted in Fig. 1. All PDFs show a sharp first peak at 2.0(2) Å, a bifurcated second peak between 2.9(0) and 4.3(0) Å, and a series of smaller peaks between 5 Å and 15 Å. Closer examination reveals a number of changes among the PDFs; the major changes, marked by letters a to f in Fig. 1, lie in the IRO. These include an increase in intensity of the peaks, appearance of new peaks, shifts in the position of the peaks and a deepening of the troughs. In most cases, the change is *systematic* with respect to the annealing temperature (see inset of Fig. (1), and remains robust when cutting the q-range of the data down to 15 $\mathrm{Å}^{-1}$.

In order to better understand the annealing-induced atomic level processes that cause the changes seen in the PDFs, it is essential to develop atomic models that are accurate enough to capture the observed changes in PDFs. A common method of choice is to follow a regression algorithm that fits atomic coordinates with the measured PDFs, e.g. simulated annealing [17] or reverse Monte Carlo (RMC) [18] etc. However, the changes caused by annealing are subtle even for the two extreme ends of annealing (viz as-deposited and 800°C annealed) and hence one faces an interesting problem and requirement: how to reliably generate two slightly different structural solutions of an otherwise identical disordered system? Conventional modeling techniques often fail to resolve subtle changes in atomic structure with high fidelity, especially in the IRO, which makes it difficult to give definitive

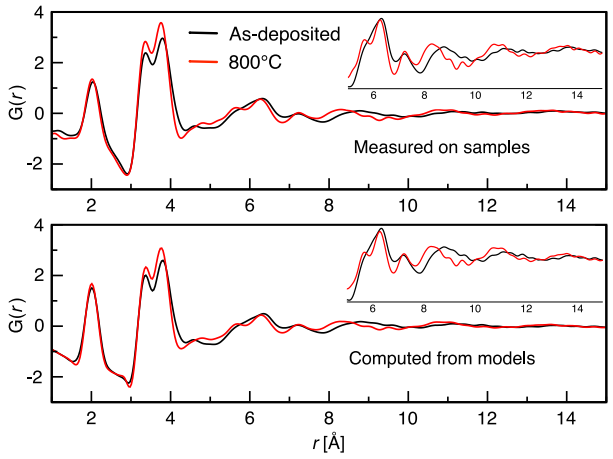

FIG. 2. **Measured and computed PDFs:** The measured PDFs from two samples (top) are compared with PDFs computed from atomic models (bottom). The PDFs highlight the ability of the atomic models to closely track the annealing-induced changes in the PDFs. Computed PDFs in the bottom plot are averages of over 1000 models. The 5 Å to 15 Å section of the PDFs are shown in higher resolution insets. See [10] for a plot of all samples.

statements about the changes in structure.

We follow an integrated modeling approach that seeks to maximally constrain the solution space by using all *a priori* information. Composition and density measurements were performed on the thin film samples to provide starting points for modeling routines (see [10]). Melt-quench molecular dynamics (MD) simulations, employing two-body empirical potentials from [19, 20], were performed at the measured composition and density to generate starting configurations for RMC. These configurations are then modified using RMC until the computed S(q) matches with the measured S(q). However, it is well known that a traditional RMC produces non-physical solutions, even in elemental systems [21]. We used *ab initio* molecular dynamics (AIMD) to generate smaller models (190 atoms) of the same system, and the distribution of bond-lengths present in the AIMD models was used as a constraint to RMC. This was achieved by requiring that the metal-oxygen bond distances lie in the range predicted by the partial PDFs of AIMD models (see [10]). Furthermore, following the "FEAR" method [22], RMC moves were interspersed with energy minimization moves iteratively until the desired agreement with experiments was obtained. The entire modeling algorithm was repeated to get 1000 independent atomic models corresponding to each of the four samples i.e. as-deposited, 300°C annealed, 600°C annealed and 800°C annealed. All the properties reported hereafter are computed by averaging over 1000 models. Fig. 2 shows the ability of the models to capture the changes on measured PDF up to 15 Å; to the best of our knowledge, it is the first demonstration that atomic models can capture changes in IRO up to 15 Å with such a high accuracy. It should be noted that the models reported in this work are chemically realistic, i.e., they contain no non-physical metal-metal chemical bonds. The models have a density and composition that are representative of the IBS coatings. We show that deductions made from the models agree with experiments, and the structural features computed from the models show a systematic trend with annealing temperature. A plot showing the fit of the S(q) and G(r) along with additional information on the modeling method is given in the supplementary material [10].

In the following, we present a discussion of the structure of a-Ta_2O_5:ZrO_2 based on the models we obtained. As in many glass-forming materials like silica, the structure of a-Ta_2O_5:ZrO_2 can be described as a 3-dimensional network of metal (M)-centred coordination polyhedra that have oxygen (O) atoms at their corners. The M-O correlation gives rise to the first peak, which is followed by a minimum at 2.9 Å that defines the M-O bond cut-off distance. The polyhedra are predominantly distorted octahedra (∼80% for Ta, ∼60% for Zr, [10]). It has been shown that the first peak of G(r) for pure a-Ta_2O_5 closely resembles the corresponding peak of crystalline Ta_2O_5 [15]. We find that the coordination of Ta by O (n_{TaO}) is 6.13 whereas n_{ZrO} is 6.14; both values are for as-deposited sample. The measured value of n_{TaO} using ^{17}O NMR studies on IBS deposited pure a-Ta_2O_5 is 6.1(3) [23, 24]. The M-O bond distance peaks at 2.0(2) Å and it is comprised of a Ta-O sub-peak at 1.98 Å and and a Zr-O sub-peak at 2.06 Å. The slight difference in Ta-O and Zr-O bond distances is also consistent with *ab initio* models; it is likely that this difference is helpful in frustrating the crystallization of tantala [9]. As a result of annealing, coordination of M by O (n_{MO}) shows a small but consistent trend to smaller values, and a corresponding change, although small, in the M-O bond distance towards a lower value is observed in the total G(r) (see Fig. 10 in [10]). The structure within the first coordination sphere of tantala has been extensively characterized [6, 15, 25, 26].

The polyhedra link with each other through O-atoms at each corner. Each O-atom is at least 2-coordinated with metal atoms. The ratio of 2-coordinated to 3-coordinated O-atoms is ∼ 1:2, which is notably different from pure tantala where the value measured using NMR is 2:3 [23, 24]. The difference comes from O-atoms bonding preferentially 3-fold with Zr; the mean O-coordination by M is 2.7 (see inset of Fig. 3(e)). The correlation between two metal atoms connected by at least one O-atom gives rise to the second peak in total G(r). It is interesting to note the bifurcation in the M-M peak into two sub-peaks at 3.35 Å and 3.75 Å since similar measurements in pure tantala show the first sub-peak at 3.35 Å at much reduced intensity [15, 25]. Its much more pronounced presence in the mixed phase is an effect of doping by zirconia and has structural implications in that the first and second peaks originate from

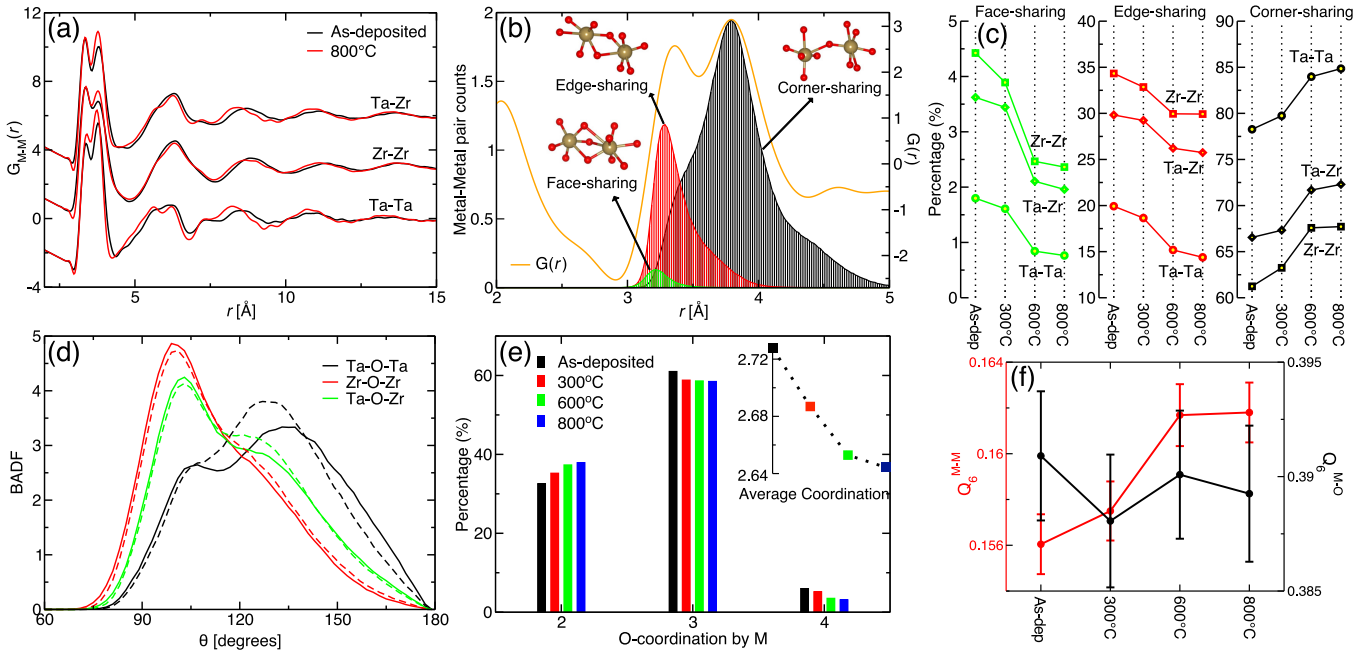

FIG. 3. **Structural fingerprints of annealing:** The major structural trends observed in the models as a function of annealing temperature are highlighted in (a) through (f): (a) partial G(r) for M-M pairs; (b) origin of the double hump in G(r) as correlations between corner and edge shared M-M pairs, where the orange line represents G(r), and the shaded regions represent the distribution of M-M distances classified as CS-, ES-, and FS-polyhedra; (c) evolution of the percentages of CS-, ES-, and FS-polyhedra; (d) BADF from the as-deposited (dashed-lines) and 800°C annealed (solid-lines) models; (e) distribution of O-coordination by M for samples with different annealing history, the inset shows the averaged coordination vs annealing temperature; (f) BOO parameters (Q_6) as a function of annealing temperature for M-O and M-M correlations (error-bars represent standard deviation).

correlations of edge-sharing (ES) and corner-sharing (CS) polyhedra respectively (Fig. 3(b)). For the as-deposited sample, the ratio of CS to ES correlations is 3.93 for Ta-Ta, 2.23 for Ta-Zr, and 1.78 for Zr-Zr. There is also a small concentration of face-sharing (FS) polyhedra where the polyhedra share three O-atoms between them.

The effect of annealing is more pronounced beyond the first M-O peak and all the way to 15 Å. Many of the changes observed in the total G(r) can be explained by considering the partial M-M correlation (Fig. 3(a)), where changes are observed from ∼3 Å up to 15 Å. The peaks become narrower and sharper suggesting that annealing increases the order in M-M correlation lengths. Since the bifurcated M-M peak represents the correlations between the polyhedra, the annealing induced change in the peak signifies that annealing alters the mode by which polyhedra connect with each other. An analysis presented in Fig. 3(c) shows that the concentration of CS polyhedra increases as a result of annealing whereas it decreases for ES and FS polyhedra. The effect of the overall decrease of density of ES and FS polyhedra is that the average O-coordination by M decreases as a function of annealing temperature (see Fig. 3(e)). A decrease in O-coordination upon annealing was also observed for pure tantala using ^{17}O NMR studies in [24]. An analysis of the M-O-M bond angle distribution function (BADF) shows that BADF, in general, narrows and shows a more defined peak upon annealing 3(d). However, there is a more characteristic change in BADF: each M-O-M BADF curve shows a double peak and the peak around 120° to 130° increases with annealing. Further analysis shows that the characteristic two-peak BADF arises from the presence of ES and CS polyhedra; the increase in M-O-M BADF around 120° to 130° is caused by increase in the ratio of CS to ES polyhedra (see Fig. 9 in [10]).

We use the bond orientational order (BOO) parameter Q_6 [27] to quantify the degree of disorder present in the models. The BOO parameter corresponding to M-O bonds, denoted by $Q_6^{\text{M-O}}$ in Fig. 3(f), shows that there is no significant effect of annealing in the M-O coordination sphere. We also probed the degree of order among the polyhedral units by computing $Q_6^{\text{M-M}}$ among the metal atoms and the values suggest an increase in BOO with annealing, a trend clearly seen in the measured G(r). To the extent $Q_6^{\text{M-M}}$ is a measure of IRO among the polyhedral units, it is noteworthy to observe an inverse correlation of $Q_6^{\text{M-M}}$ with measured values of mechanical loss at room temperature (see Fig. 1 in [10]).

A number of experiments have demonstrated that the mechanical loss of tantala-based coatings reduces at room temperature and increases at low temperature upon annealing [7, 8, 10, 28]. This effect is observed at room temperature for zirconia-doped tantala coatings similar

to those studied here, where the mechanical loss undergoes 6-fold reduction from $\sim 1 \times 10^{-3}$ in an as-deposited coating to 1.8×10^{-4} when annealed at 800°C. The low temperature mechanical loss of tantala typically produces low temperature loss peaks at around 30 K that develop and grow upon annealing [7], and has recently been observed in other zirconia-doped tantala coatings. The dissipation mechanism for mechanical loss is often conceptualized as two-level systems (TLSs) which are asymmetric double-wells separated by an energy barrier. TLSs arise from subtle rearrangements of clusters of atoms [29, 30]. The observed trends in mechanical loss with annealing suggests that ES-polyhedra are more likely associated with TLSs that contribute to room temperature mechanical loss, whereas the CS-polyhedra that form lower barrier height TLSs contribute to low temperature mechanical loss. This conjecture is bolstered by the observation that silica, which has nearly 100% CS polyhedra has low loss in room temperature and high loss at low temperature [31]. If this conjecture is correct, then in order to reduce mechanical loss at room temperature one would seek a material that has fewer ES-polyhedra and more CS-polyhedra. Conversely, a material with fewer CS-polyhedra and more ES-polyhedra would reduce mechanical loss at low temperature. As doping with zirconia helps suppress the crystallization but increases the fraction of ES-polyhedra, the doping percentage of zirconia is a key variable to optimize in order to reduce mechanical loss at room temperature. In particular, a lower concentration of zirconia that is just enough to suppress the crystallization would be desirable. In a study by Tewg *et al.* [9], lower zirconia doping concentrations in tantala were observed to suppress crystallization, with a highest crystallization temperature measured from a sample with $\mathrm{Zr}/(\mathrm{Zr}+\mathrm{Ta}) \simeq 0.33$. Investigations are currently underway for thin films with varying levels of zirconia doping concentrations.

In conclusion, we have presented a detailed study on the effect of annealing on zirconia-doped tantala amorphous thin films using a combination of experimental data and modeling routines. Upon annealing, there are subtle changes observed in the SRO, but the most significant change is the increase in IRO. The GIPDF measurement method and the modeling scheme employed in this work represent a significant step forward for the detailed study of the atomic structure of amorphous thin films, providing a powerful tool capable of accurately capturing subtle changes in the atomic structure up to 15 Å. In order to reduce coating thermal noise for Advanced LIGO +, our results and analysis indicate that an optimized zirconia doping concentration of $\mathrm{Zr}/(\mathrm{Zr}+\mathrm{Ta}) \simeq 0.33$ for a coating deposited in a similar way will further suppress crystallization and also increase the ratio of CS to ES polyhedra, and allow a maximum reduction of mechanical loss. Future modeling experiments are planned to directly compute the mechanical loss of these structures [30], which will help to quantify the change in the ratio of CS to ES polyhedra has on mechanical loss. In addition, further study of other materials that increase the ratio of CS to ES polyhedra and crystallization temperature will be important to identify other low mechanical loss coating materials, and is the subject of ongoing research.

We acknowledge the support of the LSC Center for Coatings Research, jointly funded by the National Science Foundation (NSF) and the Gordon and Betty Moore Foundation. In particular, the authors are grateful for support through NSF awards PHY-1707866 and PHY-1708175. CL, FS and RS are grateful for support from the NSERC, CFI, and FQRNT. DAD is grateful for support from NSF award DMR-1506836. IWM is supported by a Royal Society Research Fellowship. The authors are grateful to Frances Hellman and Sjoerd Roorda for useful comments and discussion. We are also grateful to Ric Shimshock at MLD Technologies for useful discussions and for providing thin film samples. We acknowledge support from Bill Baloukas and Ludvik Martinu of École Polythechnique de Montral for access to ellipsometry and stylus profilometry instruments. Use of the Stanford Synchrotron Radiation Lightsource, SLAC National Accelerator Laboratory, is supported by the U.S. Department of Energy, Office of Science, Office of Basic Energy Sciences under Contract No. DE-AC02-76SF00515. We would like to thank the Sherlock Cluster at Stanford University for providing computational resources and support that contributed to these research results.

* prasai@stanford.edu
† rbassiri@stanford.edu

[1] N. Hinkley, J. Sherman, N. Phillips, M. Schioppo, N. Lemke, K. Beloy, M. Pizzocaro, C. W. Oates, and A. Ludlow, Science **341**, 1215 (2013).
[2] G. M. Harry, H. Armandula, E. Black, D. Crooks, G. Cagnoli, J. Hough, P. Murray, S. Reid, S. Rowan, P. Sneddon, *et al.*, Applied optics **45**, 1569 (2006).
[3] S. Hild, Classical and Quantum Gravity **29**, 124006 (2012).
[4] E. Oelker, T. Isogai, J. Miller, M. Tse, L. Barsotti, N. Mavalvala, and M. Evans, Phys. Rev. Lett. **116**, 041102 (2016).
[5] L. Barsotti, L. McCuller, M. Evans, and P. Fritschel, "LIGO Technical Document T1800042 - The A+ Design Curve," `https://dcc.ligo.org/LIGO-T1800042/public` (2018).
[6] R. Bassiri, K. Borisenko, D. Cockayne, J. Hough, I. MacLaren, and S. Rowan, Applied Physics Letters **98**, 031904 (2011).
[7] I. W. Martin, R. Bassiri, R. Nawrodt, M. Fejer, A. Gretarsson, E. Gustafson, G. Harry, J. Hough, I. MacLaren, S. Penn, *et al.*, Classical and Quantum Gravity **27**, 225020 (2010).

[8] G. Vajente, R. Birney, A. Ananyeva, S. Angelova, R. Asselin, B. Baloukas, R. Bassiri, G. Billingsley, M. Fejer, D. Gibson, *et al.*, Classical and Quantum Gravity **35**, 075001 (2018).

[9] J.-Y. Tewg, Y. Kuo, and J. Lu, Electrochemical and Solid-state Letters **8**, G27 (2005).

[10] See supplementary information for additional information on the simulation method and further numerical results.

[11] S. R. Elliott, *Physics of amorphous materials* (Longman Group, 1983).

[12] S. R. Elliott, Nature **354**, 445 (1991).

[13] L. Červinka, Journal of Non-Crystalline Solids **106**, 291 (1988).

[14] M. J. Hart, R. Bassiri, K. B. Borisenko, M. Véron, E. F. Rauch, I. W. Martin, S. Rowan, M. M. Fejer, and I. MacLaren, Journal of Non-Crystalline Solids **438**, 10 (2016).

[15] B. Shyam, K. H. Stone, R. Bassiri, M. M. Fejer, M. F. Toney, and A. Mehta, Scientific Reports **6**, 32170 (2016).

[16] X. Qiu, J. W. Thompson, and S. J. Billinge, Journal of Applied Crystallography **37**, 678 (2004).

[17] S. Kirkpatrick, C. D. Gelatt, and M. P. Vecchi, Science **220**, 671 (1983).

[18] D. Keen and R. McGreevy, Nature **344**, 423 (1990).

[19] J. Trinastic, R. Hamdan, Y. Wu, L. Zhang, and H.-P. Cheng, The Journal of Chemical Physics **139**, 154506 (2013).

[20] J. Yu, R. Devanathan, and W. J. Weber, Journal of Materials Chemistry **19**, 3923 (2009).

[21] D. Drabold, The European Physical Journal B **68**, 1 (2009).

[22] A. Pandey, P. Biswas, and D. A. Drabold, Scientific Reports **6**, 33731 (2016).

[23] N. Kim and J. F. Stebbins, Chemistry of Materials **23**, 3460 (2011).

[24] N. Kim and J. F. Stebbins, Journal of Non-Crystalline Solids **378**, 158 (2013).

[25] O. L. Alderman, C. Benmore, J. Neuefeind, E. Coillet, A. Mermet, V. Martinez, A. Tamalonis, and R. Weber, Physical Review Materials **2**, 043602 (2018).

[26] R. Bassiri, F. Liou, M. R. Abernathy, A. C. Lin, N. Kim, A. Mehta, B. Shyam, R. L. Byer, E. K. Gustafson, M. Hart, *et al.*, APL Materials **3**, 036103 (2015).

[27] P. J. Steinhardt, D. R. Nelson, and M. Ronchetti, Physical Review B **28**, 784 (1983).

[28] G. M. Harry, M. R. Abernathy, A. E. Becerra-Toledo, H. Armandula, E. Black, K. Dooley, M. Eichenfield, C. Nwabugwu, A. Villar, D. Crooks, *et al.*, Classical and Quantum Gravity **24**, 405 (2006).

[29] P. Fedders and D. Drabold, Physical Review B **53**, 3841 (1996).

[30] J. P. Trinastic, R. Hamdan, C. Billman, and H.-P. Cheng, Physical Review B **93**, 014105 (2016).

[31] K. Topp and D. G. Cahill, Zeitschrift für Physik B Condensed Matter **101**, 235 (1996).